Analysis of RyR2 distribution in HEK293 cells and mouse cardiac myocytes using 3D MINFLUX microscopy

Alexander H Clowsley[1*], Anna Meletiou[1*], Evelina Lučinskaitė[1], Isabelle Jansen[2], Peter P. Jones[3], William E. Louch[4,5], Christian Soeller[1, Δ]

Affiliations

[1]Department of Physiology, University of Bern, Bern, Switzerland.
[2]Abberior Instruments, Hans-Adolf-Krebs-Weg 1, 37077 Göttingen, Germany.
[3]Department of Physiology, School of Biomedical Sciences and HeartOtago, University of Otago, Dunedin, New Zealand.
[4]Institute for Experimental Medical Research, Oslo University Hospital and University of Oslo, Oslo, Norway.
[5]K.G. Jebsen Centre for Cardiac Research, University of Oslo, Oslo, Norway.
*These authors contributed equally.
Δ Corresponding author: christian.soeller@unibe.ch

Abstract

The cardiac type 2 ryanodine receptor (RyR2) is a large homotetramer of a ~560 kD subunit and is the molecular pathway through which the majority of Ca^{2+} enters the cytosol during cardiac activation. It constitutes the molecular basis of the process of calcium induced calcium release where activation of RyR2s can be locally regenerative giving rise to local release events termed Ca^{2+} sparks. Accordingly, the molecular distribution of RyR2 in cardiac myocytes has been of great interest. Here we present the first purely optical data of RyR2 distribution with sub-molecular resolution by applying 3D MINFLUX fluorescence super-resolution microscopy. We demonstrate that by using single-domain antibodies (sdABs) against fluorescent protein domains in engineered RyR2 fluorescent protein fusions we can determine the location of individual RyR2 subunits with high precision (~3 nm) in all directions. This allows determining not only the location but also the 3D orientation of individual RyR2 channels in intact cells. In practice, this capability is currently limited by a relatively modest effective labeling efficiency (~10 % subunit detection efficiency translating into ~35% RyR2 labeling efficiency) which we measure *in-situ* using a novel procedure enabled by the true molecular resolution of MINFLUX microscopy. The new data suggests a resolution to apparent discrepancies between previous data from electron microscopy and super-resolution data that may be at least partially explained by effects of labeling efficiency. The methodology developed here will be critical to reveal the full complexity of RyR2 and related Ca^{2+} handling proteins in 3D as well as their relationship to contractile function. Our new approaches may be applicable to other multi-subunit complexes in cardiac muscle and other cell types.

Introduction

The large (~2.3 MDa) cardiac type 2 ryanodine receptor (RyR2) protein acts as a calcium channel and controls Ca^{2+} release from intracellular stores. It is now well-established that the organisation of RyR2s into adjacent groups of channels or "clusters" is an important modulator of Ca^{2+} release in cardiac ventricular myocytes (VMs), and thus cardiac contractile function. Using conventional super-resolution imaging we and others have shown that RyR2s are organised into clusters of widely varying sizes (with an average size of ~10 RyR2s[1,2]), and that these form the molecular basis of Ca^{2+} release[1,3]. The 3D arrangement of RyR2 tetramers within clusters has been shown using 3D electron microscopy to be highly variable[4,5], exhibiting both adjoining and oblique interactions[6] that may affect the gating of interacting RyR2s.

Optical super-resolution imaging of RyR2s has become an important assay technique to characterise the malleable relationship between subcellular RyR2 distribution at the nanoscale and local, as well as cell wide Ca^{2+} release. For example, RyR2 dispersion, a nanoscale RyR2 rearrangement that includes fragmentation of RyR2 groupings into more numerous, smaller clusters, without any change in overall channel number, was first observed in myocytes from failing hearts using dSTORM super-resolution imaging[7]. Similarly, nanoscale ryanodine receptor configurations were correlated to calcium sparks in cardiomyocytes using live cell photoactivated localization microscopy (PALM)[8]. A similar approach correlated functional Ca^{2+} signals and *in-situ*

fixed myocytes imaged with DNA-PAINT[9]. Despite the strong impact that optical super-resolution imaging of RyR2s in ventricular myocytes has had to date, several critical issues remain. While the importance of the relative orientation of RyR2s has been suggested by previous EM studies[4,5], non-equivocal determination of RyR2 orientations using optical super-resolution imaging has remained elusive. Similarly, there are some apparent discrepancies between data from optical super-resolution imaging of RyR2s and 3D EM studies. While EM studies suggest a fairly close packing of RyR2s in larger clusters[4,5], RyR2 clusters imaged with optical super-resolution methods seem more sparsely filled with receptors[2].

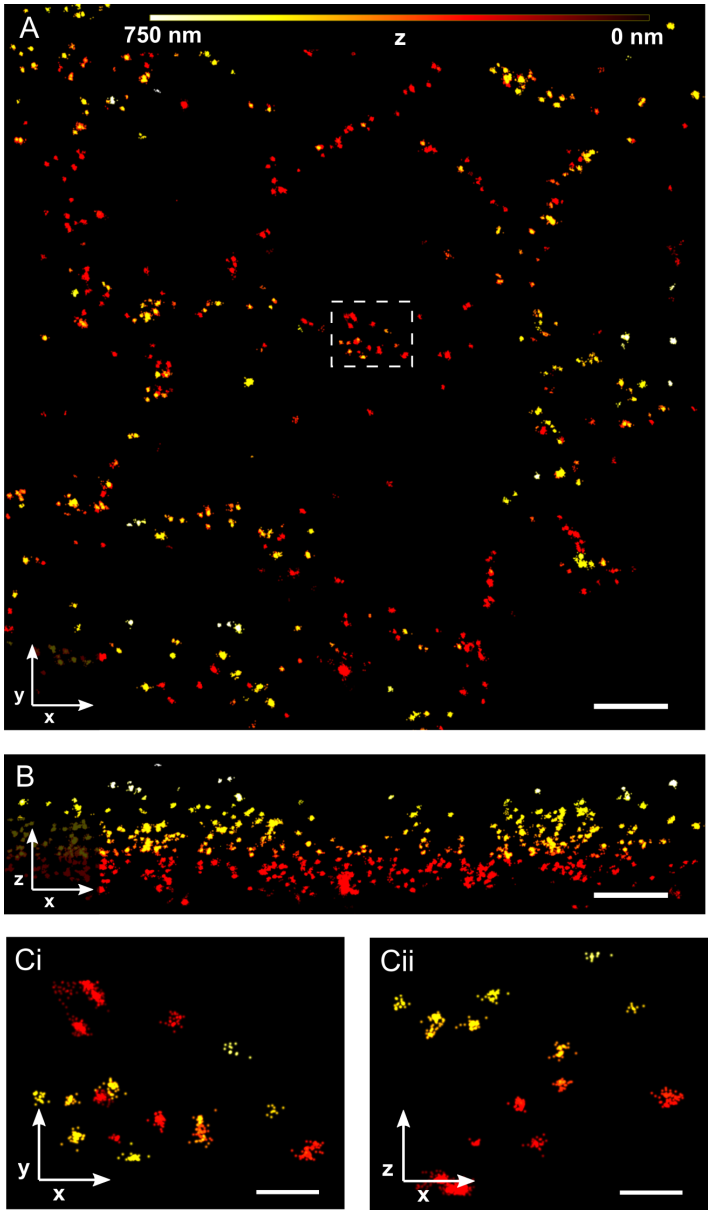

Figure 1. 3D MINFLUX images of RyR2 sdAB labeling in HEK293 cells. **A**. x-y overview of anti-GFP sdAB labeled RyR2s in a HEK293 cell stably expressing $RyR2_{D4365\text{-}GFP}$. **B**. The corresponding x-z view illustrates the complex 3D distribution of the localizations. **C**. A small region, indicated in A, shows that localizations that appear adjacent in an x-y view (Ci) are well-separated along the z-axis (Cii). Color indicates z-elevation, the renderings show raw MINFLUX localizations. Scale bars A, B: 500 nm; Ci-ii: 100 nm.

Recently, more advanced optical super-resolution imaging approaches have become available, that have demonstrated truly molecular resolution approaching the single digit nanometer scale in biological samples[10,11]. MINFLUX microscopy pairs that with full, near-isotropic 3D resolution using a single objective[12] and so we examined if MINFLUX 3D imaging of RyR2s would allow some of the issues mentioned above to be overcome.

Here we show that MINFLUX 3D imaging of RyR2s when combined with a small marker approach can, in principle, determine RyR2 3D orientations in intact cells. We establish a new *in-situ* approach to estimate effective labeling efficiency which helps resolve some of the apparent discrepancies with EM data, which we re-examine in light of the new 3D MINFLUX data. We show the first fully isotropic 3D light microscopy data of RyR2s in HEK293 cells and mouse ventricular myocytes where localization precision is better than 3 nm in all directions.

Results

3D MINFLUX imaging of RyR2s in HEK293 cells

An important consequence of using MINFLUX microscopy for the 3D imaging of RyR2s becomes apparent in 3D views of the labeling distribution in HEK293 cells expressing RyR2s (more specifically, an RyR-GFP fusion protein $RyR2_{D4365\text{-}GFP}$ as previously characterised[13]), as shown in Fig. 1. To visualise RyR2s using MINFLUX imaging the cells were stained with single domain antibodies (sdABs or "nanobodies") against GFP that was conjugated to Alexa-Fluor 647. Notably, the 3D MINFLUX data has nearly isotropic resolution in all three dimensions, which has previously generally required more complex 4PI microscopy with opposing objectives[14].

As expected, the distribution pattern of RyR2 labeling reflects the tubular ER morphology (Fig. 1A, x-y view), and its highly three-dimensional architecture is apparent in x-z views (Fig. 1B). The importance of 3D information is emphasized by inspection of a small image region that in an x-y view appears to show a group of adjacent RyR2s (Fig. 1Ci). In the x-z view it becomes clear that several apparently proximal "RyR2 puncta" are several hundred nanometers apart in the axial

direction (z, Fig. 1Cii). This high 3D precision is critical when determining cluster groupings of adjacent RyR2s as we show further below.

Estimating RyR2 tetramer subunit locations

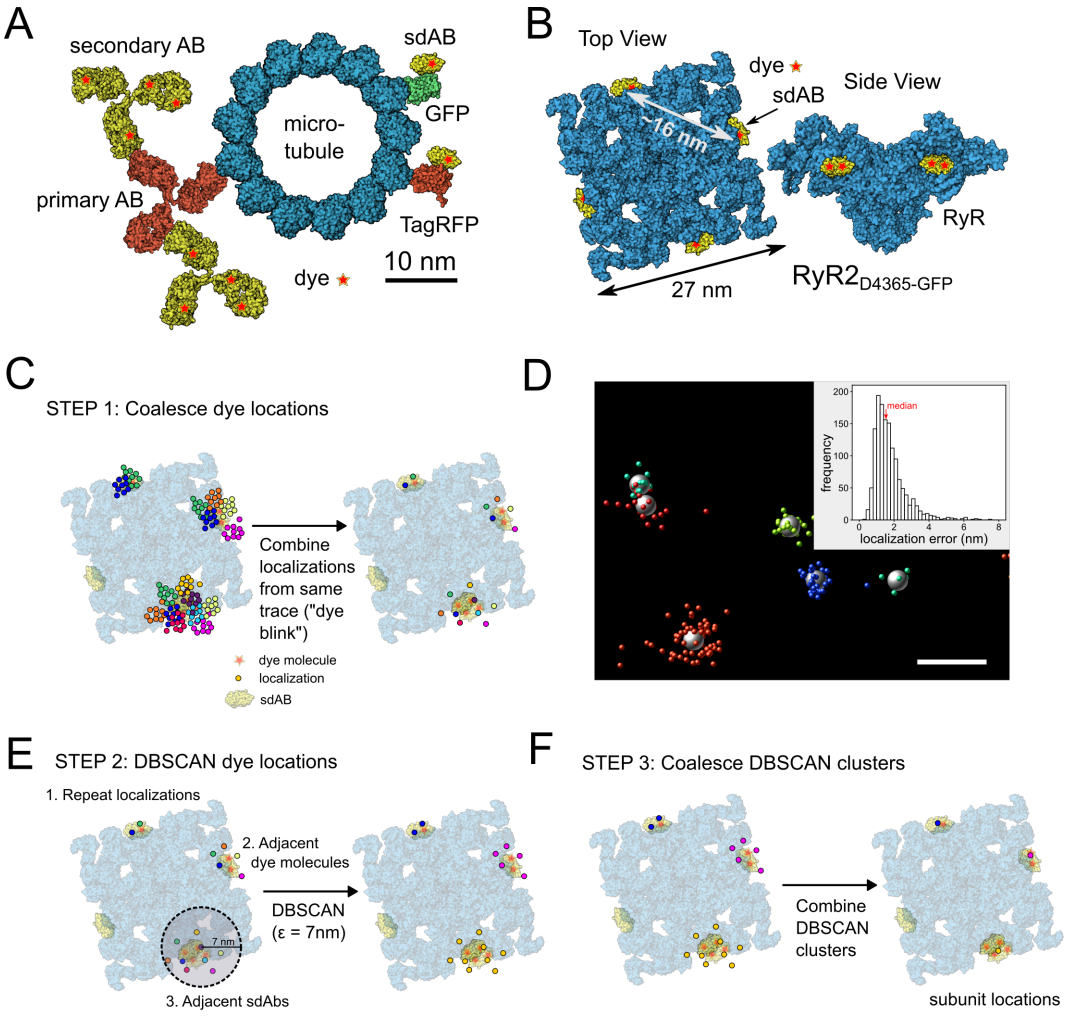

Figure 2. Marker systems for RyR2 MINFLUX imaging and processing of raw MINFLUX localizations to obtain "subunit locations". **A.** Schematic of relative target and marker sizes showing a primary/secondary AB labeling approach versus a GFP-sdAB or TagRFP-sdAB approach. A microtubule in cross-section illustrates target protein size (diameter ~25nm) which is similar to the size of RyR2 (panel inspired by reference [15]). **B.** Schematic of $RyR2_{D4365\text{-}GFP}$ with approximate locations of anti-GFP sdAB binding sites according to structural data from reference [19]. **C.** Step 1 of the algorithm to estimate subunit locations. Raw MINFLUX localizations from the same dye "blink" (identified by localisations with the same trace ID) are combined to obtain dye locations. **D.** Small region of MINFLUX data that shows raw localizations (small colored spheres) where color indicates the dye molecule "trace"; combined localizations from the same trace are shown as grey spheres in 3D. The inset shows the z localization error of the combined localizations with a median of 1.5 nm. **E.** Step 2 of the algorithm – repeated dye locations from dye blinking, adjacent dye molecules and dye locations from adjacent sdABs are grouped using DBSCAN clustering with eps = 7 nm. **F.** Step 3 of the algorithm – dye locations in groups determined in Step 2 are combined to obtain subunit location estimates, with each location corresponding to a unique subunit. Scale bars D: 50 nm.

The considerably higher localization precision accessible with MINFLUX microscopy prompted us to consider marker systems available to visualize RyR2s with fluorescence super-resolution microscopy, since the size of some marker combinations may defeat the purpose of achieving truly molecular resolution[15]. Labeling RyR2s with primary and secondary antibody (AB) labeling systems while aiming for molecular imaging resolution is complicated by the considerable size of IgG molecules (7-12 nm, Fig. 2A, see also Supp. Fig. 1). By contrast, the use of single domain antibodies (sdABs) in conjunction with suitable targets such as relatively compact fluorescent proteins (FPs) should encounter smaller linkage errors, on the order of ~3-4 nm (Fig. 2A). This approach is compatible with RyR2 FP fusion proteins that include GFP or similar FPs. Specifically, insertion of GFP after residue D4365 has been previously performed and the resulting $RyR2_{D4365\text{-}GFP}$ has been shown to be functionally essentially indistinguishable from wild type RyR2[13]. The locations of the inserted GFPs (4 GFPs

per tetramer) were previously localized by single particle cryoEM and found to be arranged on the corners of a square with ~16 nm length that is oriented at nearly 45 degree to the square outline of the tetramer itself[13] (Fig. 2B). Imaging HEK293 cells stably expressing $RyR2_{D4365\text{-}GFP}$ stained with an sdAB against GFP we could localize Alexa 647 dye molecules conjugated to these sdABs with high precision in 3D. Given the relatively small size of sdABs we aimed to localize individual subunits of a RyR2 tetramer.

To obtain estimates of unique locations of RyR2 subunits, raw MINFLUX localizations (as visualised in Fig. 1) were processed by a multistep procedure to eventually obtain estimates of individual "subunit locations", broadly similar to a previous approach to assign MINFLUX localizations to stained molecules[12]. In a first step, to achieve high localization precision, repeated MINFLUX localizations from the same dye molecule "blink" (identified by the same MINFLUX "trace ID" – parameter TID[16]) were combined[12,16] to obtain what represents individual dye locations (Fig. 2C). Each dye location obtained in this way will have originated from a single dye molecule on an sdAB. Closely adjacent dye locations may have originated from the same dye molecule due to repeated "blinking" during MINFLUX data acquisition, a possibility we consider in step 2 of the processing pipeline. The combination of raw MINFLUX localizations in step 1 results in dye locations with a median precision of better than 2 nm in all three-dimensions, see Fig 2D (for localization precisions in all three dimensions and resolution measurements see, Supp. Fig. 2). As shown in Fig. 2C, after combining localizations from the same trace there may still be several dye locations originating from the same subunit. In step 2 we therefore group dye localizations that likely belong to the same subunit. This is achieved by DBSCAN clustering with ε = 7 nm, see Fig. 2E. The distance was determined from simulations of dye locations that take the labeling geometry by sdABs and the measured localization errors into account (Supp. Fig. 3). The DBSCAN radius ε was chosen to be large enough to group most dye locations originating from markers on the same RyR2 subunit and sufficiently small to not incorrectly merge dye locations from adjacent subunits on the same RyR2 tetramer (or closely adjacent RyR2 tetramers). With this value of ε we have estimated in simulations that such errors occur in fewer than 1% of cases (Supp. Fig. 4 and Supp. Methods). Step 2 aims to group dye locations that (1) arose from dye molecules that reappear due to blinking, as mentioned above, or (2) correspond to dye molecules on the same sdAB or, finally, (3) arose from two sdABs bound to the same GFP domain (the X4 nanotag sdABs contain 2 types of sdABs against different epitopes).

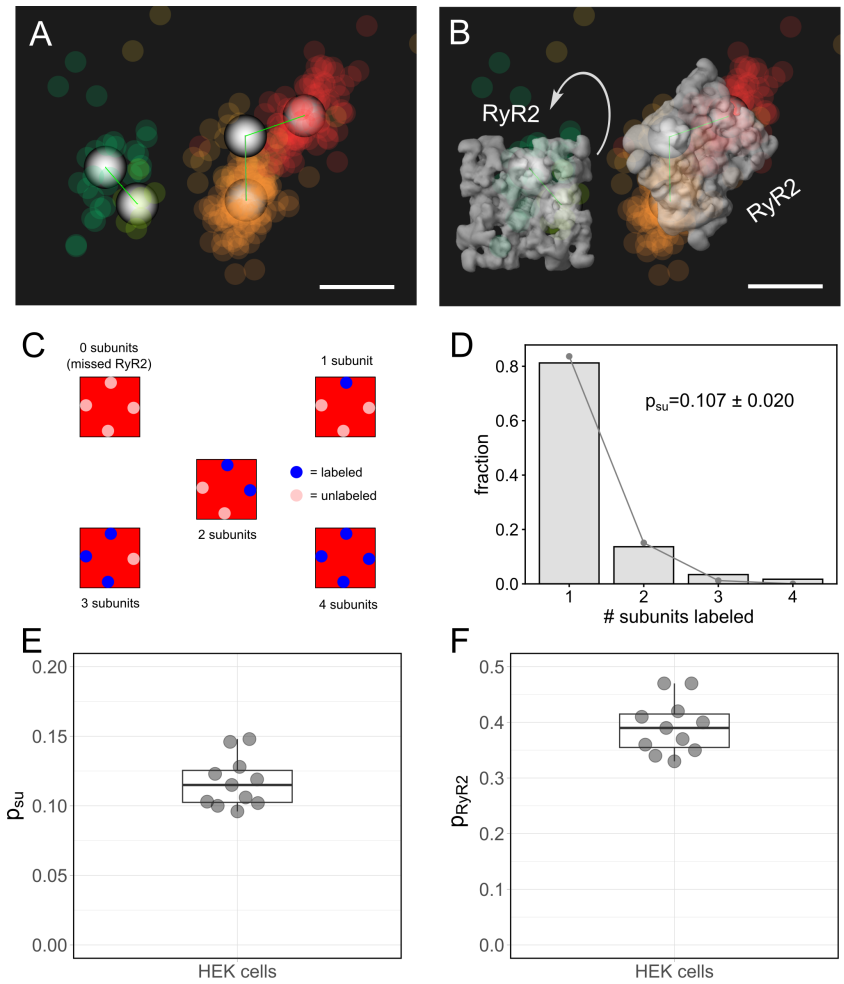

Figure 3. Effective labeling efficiency of sdAB labeled $RyR2_{D4365\text{-}GFP}$. **A**. Illustration of subunit localizations (grey spheres) in a small region of a HEK293 cell expressing $RyR2_{D4365\text{-}GFP}$. Corresponding raw MINFLUX localizations are shown by trace ID color. The green lines highlight nearest neighbor subunit distances which are 15-20 nm. **B**. The arrangement of subunit localizations in A is compatible with RyR2 tetramers arranged in 3D as indicated. Since only two subunits are localized, the tetramer on the left leaves rotation around the indicated axis (arrow) undetermined. **C**. Schematic showing some of the possible arrangements as 0-4 subunits of an RyR2 tetramer are labeled. **D**. Comparison of the fraction of labeled subunit groups in a MINFLUX dataset fit with binomial theory, best fit values as indicated in the figure. **E**. Subunit labeling efficiency estimates p_{SU} from 11 datasets (4 independent repeats). **F**. Corresponding probability p_{RyR2} of detecting an RyR2 tetramer (i.e. at least one subunit labeled). Scale Bars A, B: 20 nm.

Finally, in step 3, dye locations grouped into the same DBSCAN cluster are combined to arrive at a single subunit location estimate for each labelled subunit (Fig. 2F). Our simulations using typical localization errors (Fig. 2D, inset), expected sdAB labeling geometries as well as a variety of RyR2 tetramer arrangements suggest that errors arising from the subunit combination procedure occur in only 5-10 % of all cases (Supp. Fig. 4). We proceeded to further analyse the three-dimensional distribution of the resulting *subunit locations*, a term we will use throughout the remainder of the study, with the aim to achieve new insights into the underlying RyR2 tetramer distribution.

RyR2 tetramer orientation and estimates of effective labeling efficiency

We hypothesized that small groups of adjacent subunit localizations that we observed in MINFLUX data sets of $RyR2_{D4365\text{-}GFP}$ labeled with anti-GFP sdABs might represent adjacent subunits of the same $RyR2_{D4365\text{-}GFP}$ tetramer (see also Fig. 2B). The subunit locations shown in Fig. 3A are examples compatible with the presence of RyR2 tetramers oriented in 3D, as indicated in Fig. 3B. Notably, when at least 3 subunits of a tetramer are labeled and detected this allows the 3D orientation of an RyR2 to be estimated with reasonable precision. Two labeled subunits leave at least one axis of rotation undetermined (see also Fig. 3B). Occasionally, arrangements of 4 adjacent subunit locations compatible with a fully labelled RyR2 tetramer were observed, see an example in Supp. Fig. 5. While determining the 3D orientation of RyR2s is a new ability enabled by the high localization precision of 3D MINFLUX imaging with a small marker system, inspection showed that datasets

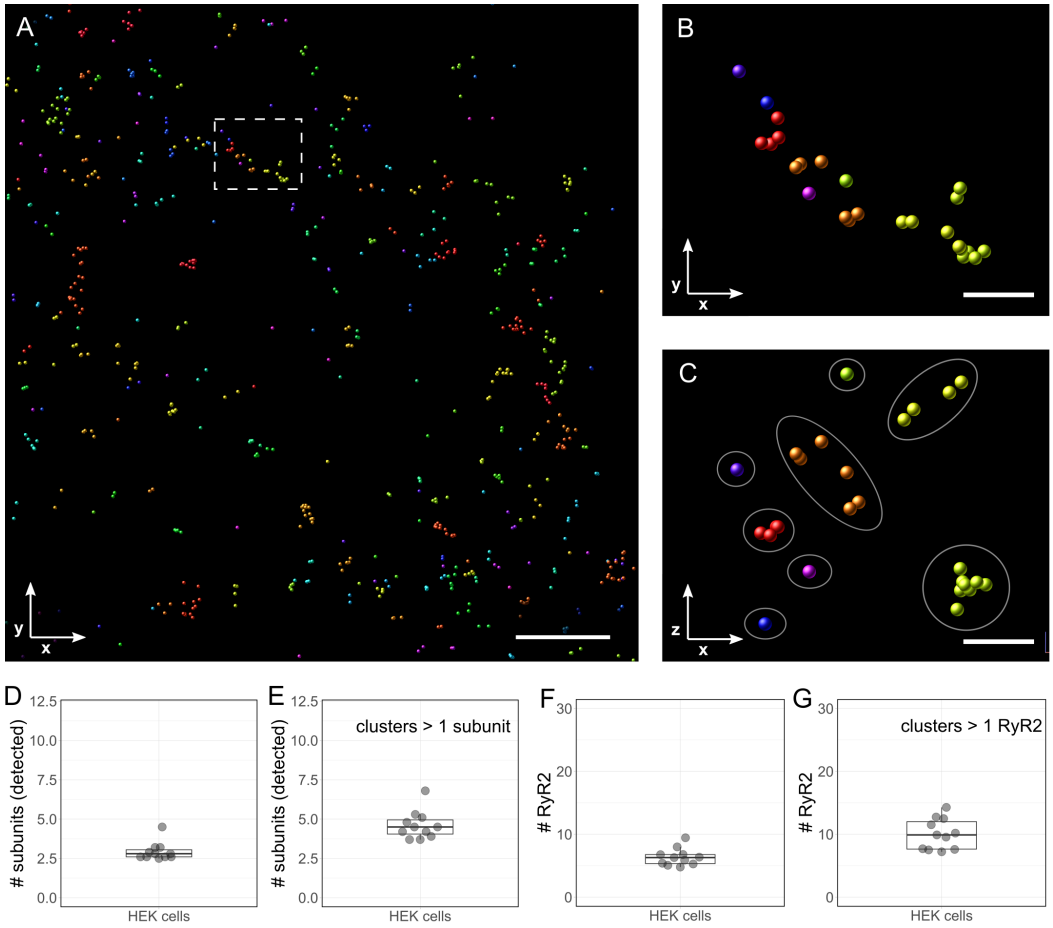

Figure 4. Clustering of RyR2 subunit localizations in HEK293 cells. **A**. Overview of RyR2 subunit clustering in a HEK293 cell expressing $RyR2_{D4365\text{-}GFP}$. Clustering was determined with dbscan (eps = 100 nm) and using the 3D coordinates of subunit locations. Coloring indicates locations belonging to the same cluster. **B**. Subunit locations in a small region (rectangle in A) appear to be closely grouped in an x-y view. **C**. When viewed in an x-z view the large spread along z becomes clear which explains subunits grouping into different clusters (cluster groupings are indicated by the surrounding ellipses). **D**. Mean subunit cluster size (n=11 cells, 4 independent repeats). **E**. Mean subunit cluster size for all clusters containing at least 2 subunits. **F**. Mean number of RyR2s in a cluster, extrapolated from number of subunits and corrected for labeling efficiency. **G**. Mean number of RyR2s in cluster containing at least 2 RyR2s, corrected for labeling efficiency. Scale bars A: 500 nm; B, C: 100 nm.

contained only a relatively small fraction of these proximal multi-subunit location groupings. Most molecules were isolated with nearest neighbor subunit locations 30 nm or further from each other. Since sdABs are 3-4 nm in size[17] and the GFP residues in a $RyR2_{D4365\text{-}GFP}$ tetramer are ~16 nm from each other we would not expect steric effects to play a major role. Thus, assuming the probability of sdABs binding at adjacent subunits of a $RyR2_{D4365\text{-}GFP}$ tetramer being statistically independent, binomial theory predicts the fractions given an effective subunit labeling probability p_{su}, based on the possibility of an $RyR2_{D4365\text{-}GFP}$ tetramer having 0, 1, 2, 3 or 4 of their GFPs labeled, Fig. 3C. In the MINFLUX data sets we determined the fraction of 1, 2, 3 or 4 subunit containing groups using an algorithm that counts subunit locations in suitable proximity to arise from the same RyR2 tetramer (see supplementary methods) and comparison of the estimated fractions with a binomial distribution showed good agreement when p_{su} was about 10% (Fig. 3D, best fit for the data set shown was p_{su} = 0.107±0.020). We validated this algorithm using simulated subunit locations (see supplementary methods and Supp. Fig. 6) which suggested good agreement between the estimate of p_{su} and the underlying probability p_{su} used in the simulations. Pooling of MINFLUX datasets (11 datasets, 4 independent repeats) yielded an estimated mean p_{su} of 0.118 ± 0.005, corresponding to an effective RyR2 labeling efficiency (i.e. at least 1 subunit labeled) of 0.39 ± 0.01 (Fig. 3E-F). This effective labeling efficiency not only results from the "chemical" labeling efficiency of the sdABs but is potentially further lowered by the requirement to localize an attached dye molecule with high precision in MINFLUX imaging. Regardless of the magnitude of the labeling efficiencies the important advance of MINFLUX imaging of RyR2s analysed in this way is the intrinsic availability of a quantitative labeling efficiency estimate.

RyR2 clustering in HEK293 cells determined from MINFLUX subunit location estimates

We conducted a cluster analysis of RyR2s in HEK293 cells using the subunit localization estimates as well as the estimated labeling efficiency for quantitative corrections. To determine groupings of RyR2s (represented by detected subunit locations) that may be at a distance to effectively cross-talk via their released Ca^{2+}, we carried out dbscan clustering of subunit locations. In choosing an appropriate distance regime for RyR2 cluster determination we considered both the signalling distance over which adjacent RyR2s may effectively activate each other (on the order of 100 nm) and also took into account the new information from our data that only a fraction of all subunits are labelled. Given that we detect only 10-15% of all subunits in the MINFLUX data, our simulations indicate that a distance ε of 100 nm is needed to avoid artificially fragmenting "tight" RyR2 clusters that would be correctly grouped with ε = 40 nm if labeling were near complete (see Methods and Supp. Fig. 7). We therefore adopted a distance ε of 100 nm as search radius as a compromise that would reconstruct underlying tight groupings of RyR2s mostly correctly and is also compatible with estimated signalling distances (see also Discussion). The high 3D precision of subunit positions turned out to be critical when determining cluster groupings of adjacent RyR2s (Fig. 4A). Subunit locations were often grouped in different clusters where groups of locations that appeared to be adjacent in an x-y view (Fig. 4B) turned out to have large z distances when viewed along z (Fig. 4C). Statistical analysis showed that a cluster contained on average 2.94±0.18 subunits (Fig. 4D). Since many of these "clusters" merely contain a single subunit (see histograms in Supp. Fig. 8) we also calculated the mean number of subunits in clusters that contain at least 2 subunits. This increased the mean cluster size to 4.61±0.27 subunits, illustrating the effect of a large number of "isolated" subunit locations (reflecting isolated RyR2s) (Fig. 4E). Since every RyR2 tetramer has 4 subunits it would seem obvious that the number of RyR2s in a cluster is then simply obtained by dividing the number of subunit locations in a given cluster by 4. However, this would ignore the effective labeling efficiency we determined with the approach described above. With the estimate of p_{SU} we therefore applied a correction to extrapolate to the actual number of RyR2s in these clusters (see Methods) which yielded a mean cluster size of 6.34±0.42 RyR2s (Fig. 4F) and a mean size of 10.0±0.74 RyR2s for non-isolated receptor clusters (Fig. 4G). This demonstrates the value of an intrinsic estimate of p_{SU} for each data set as labeling efficiency may vary between experiments and laboratories and as a previously uncontrolled variable might have biased comparisons.

MINFLUX imaging of RyR2s in ventricular myocytes

Using the recently characterized PA-RFP RyR2 knock-in mouse line[18] we also carried out MINFLUX imaging of RyR2s in isolated ventricular myocytes. Myocytes from PA-RFP RyR2 mice express $RyR_{T1365\text{-}PATagRFP}$, an RyR2 with tagRFP insertion at the equivalent site to the previously structurally characterized $RyR_{1366\text{-}GFP}$[19]. PA-RFP RyR2 mouse myocytes were labeled with an anti-tagRFP sdAB conjugated to Alexa 647 as a suitable small

marker system. Confocal imaging was used to localize peripheral couplings at the surface sarcolemma (Fig. 5A, B) and select small regions for MINFLUX imaging. Note that we focus here on surface couplings as the current operation of the MINFLUX long-term sample tracking unit (see Methods) currently requires fiducial gold beads to be in focus which limits highest stability MINFLUX imaging to the immediate vicinity of the coverslip interface. When switching into MINFLUX imaging mode the blurred regions likely representing RyR2 clusters in the confocal image (Fig. 5B) were clearly resolved into punctate groups of localizations (Fig. 5C). Using the subunit assignment approach described above followed by dbscan clustering of the obtained 3D subunit localizations, the underlying RyR2 clusters were clearly revealed in 3D as shown in both x-y (Fig. 5D) and x-z views (Fig. 5E). Notably, this includes a number of large peripheral clusters containing > 30 subunits. Although peripheral couplings are close to the surface sarcolemma, the associated RyR2 distributions exhibit significant 3D structure with peripheral couplings deviating from 2D plane arrangement (see also Supp. Fig. 9). Fig. 5F and 5G show an illustrative example where a cluster extends over several hundred nanometers away from the surface membrane.

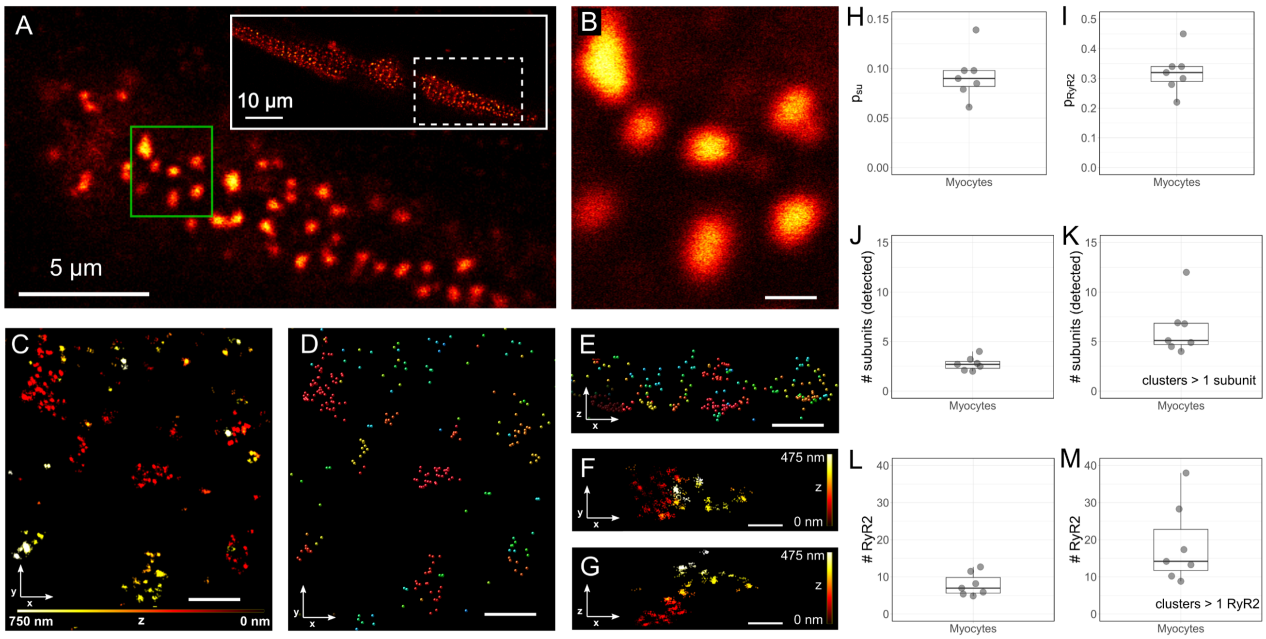

Figure 5. MINFLUX imaging of RyR2s in myocytes from PA-RFP RyR2 knockin mice. **A**. RyR2 distribution in an isolated myocyte from a PA-RFP RyR2 mouse, stained with an anti-tagRFP sdAB and imaged in the confocal mode of the MINFLUX microscope. **B**. A region at the surface sarcolemma (green rectangle in A) was selected for MINFLUX 3D imaging. **C**. MINFLUX 3D image of the region shown in B, localizations are colored by z coordinate. **D**. The subunit localizations determined from the raw MINFLUX localizations in C after dbscan clustering; coloring indicates cluster groupings. **E.** x-z view of the clusters shown in D. **F**, **G**. x-y and x-z view of a cluster illustrating the axial extent of peripheral clusters. **H**. Subunit labeling efficiency estimates p_{SU} from 7 cells, from 3 different animals. **I**. Corresponding probability p_{RyR2} of detecting an RyR2 tetramer. **J**. Mean number of subunits in a cluster (n=7 cells, 3 animals). **K**. Mean subunit numbers in a cluster for all clusters containing at least 2 subunits. **L**. Mean number of RyR2s in a cluster, corrected for labeling efficiency. **M**. Mean number of RyR2s in a cluster containing at least 2 RyR2s, corrected for labeling efficiency. Scale bars B-E: 500 nm; F, G 200 nm.

The locations of the TagRFP insertion at T1365 map to a square with side length of ~20 nm that is approximately aligned with the four "corners" of the intact RyR2 tetramer[19] (see also Supp. Fig. 10). As with the HEK293 cell data we therefore carried out an analysis of effective labeling efficiency which resulted in an estimate p_{SU}=0.093 ± 0.009 (data from 7 cells and 3 animals, Fig. 5H), broadly similar but slightly lower than the estimated labeling efficiency in HEK293 cells (two sample t-test, p=0.03). This is equivalent to an RyR2 detection probability of 0.32±0.03 (Fig. 5I), in other words, about a third of all RyR2s are labeled. Conducting DBSCAN clustering (ε = 100 nm as described above, see also Supp. Fig. 7) the average cluster contains 2.75±0.26 subunit locations and the average cluster that contain at least 2 subunit locations contains 6.32±1.04 subunit locations. Applying a correction based on the estimated effective labeling efficiency, as carried out with the HEK293 cell data sets above, this corresponds to a mean cluster size of 7.91±1.17 RyR2s for all clusters and 18.6±4.1 RyR2s for clusters with at least 2 RyR2s (Fig. 5J-M).

Relationship of MINFLUX data to previous EM tomography data

Our observations that fluorescent imaging may only detect a subset of all RyR2s in a myocyte suggests that apparent discrepancies between prior super-resolution data and EM tomography data of RyR2 clusters should be re-examined in light of our new findings. To test this idea we retraced EM tomography data from two previous studies[4,20] and used the obtained RyR2 cluster morphologies as the starting point to represent close to 100% detection efficiency of RyR2s (with the caveat that EM tomography may achieve this only for larger RyR2 clusters, small groups of RyR2s may be less sensitively detected, see discussion). The traced RyR2 cluster layouts were used to generate corresponding TagRFP locations (see also Supp. Fig. 10) and then simulate a subunit detection efficiency close to 10%. Randomly selected subunit locations (blue dots in Fig. 6A) according to this procedure were used to mimic MINFLUX subunit localizations by also adding 3D localization errors with a standard deviation of ~3 nm. The resulting "simulated" subunit clusters (Fig. 6 Bi,ii) resembled qualitatively the larger subunit localization clusters in our MINFLUX 3D RyR2 data obtained in myocytes (Fig. 6 Biii,iv). As a

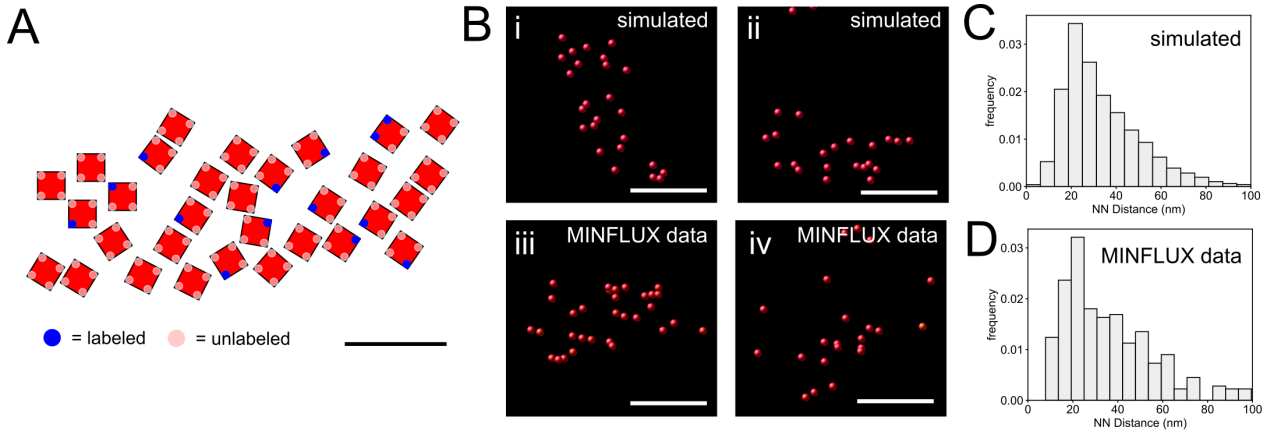

Figure 6. Comparison of MINFLUX 3D RyR2 data with cluster morphologies from EM tomography data. **A**. RyR2 positions determined by EM tomography as traced from reference [4], Fig. 1 therein, overlayed with the locations where sdABs can bind to TagRFP residues (see also Supp. Fig. 10). From all possible binding positions "labeled" positions were selected randomly (shown as blue dots) with a probability p_{SU} = 0.1. **B**. 3D localization errors (σ=3 nm) were added to generated labeled subunit positions to generate "simulated" subunit clusters (i,ii) which appear qualitatitevly similar to actual MINFLUX 3D subunit clusters (iii,iv). **C**. Histogram of nearest neighbor distances between simulated subunit cluster localizations as in B(i,ii). **D**. Histogram of nearest neighbor distances between localizations in "large" MINFLUX 3D clusters (containing at least 5 subunit locations). Scale bars A: 100 nm; B: 200 nm.

more quantitative measure we determined the nearest neighbor (NN) subunit localization distances in both these "simulated" clusters and clusters in our MINFLUX 3D myocyte data, restricting analysis to larger subunit clusters. The resulting nearest neighbor distance histograms bears a strong resemblance to each other (Fig. 6C and Fig. 6D), further supporting the idea that the MINFLUX sdAB based imaging of RyR2s may "subsample" the underlying RyR2 distribution with the estimated labeling efficiency.

To address the question if the observed non-complete labeling is purely a property of the sdAB labeling system used here, we carried out a comparison of labeling approaches using widefield DNA-PAINT super-resolution imaging. DNA-PAINT imaging previously achieved the highest resolution among "conventional" optical super-resolution microscopy methods. In these previous studies, RyR2 positions were estimated from the location of punctate DNA-PAINT labeling in 2D rendered super-resolution images. We produced such images using (1) DNA-PAINT data of sdAB labeled PA RFP RyR2 mouse myocytes versus (2) DNA-PAINT data of primary/secondary AB labeled RyR2s in mouse ventricular myocytes. When these images were analysed using a "blob" finding algorithm, similar as done previously[2], the nearest neighbor distance distributions of "blobs" (previously identified as RyR2 positions) were comparable (Supp. Fig. 11) with a median nearest neighbor distance between puncta of 34 versus 38 nm (ABs vs sdABs) that was not significantly different (p=0.66). This suggests that the sdABs used in our MINFLUX imaging experiments have *per se* a broadly comparable RyR2 labeling efficiency as other antibody labeling systems used previously. The amplification available in primary-secondary AB labeling (due to several docking sites per secondary AB and possible multiple binding) should have a negligible effect on puncta distances, since due to the lower DNA-PAINT resolution (typically ~24 nm FRC resolution) these should all be merged into the same punctum. We also rendered MINFLUX myocyte data into 2D super-resolution images and analysed these with the same blob finding approach. In these MINFLUX

2D super-resolution images the median nearest neighbor distance between puncta was ~42 nm (significantly larger than distances from DNA-PAINT imaging both with ABs and sdABs, p=0.003 and p=0.007, respectively), slightly larger than in the corresponding sdAB DNA-PAINT data, compatible with the idea that the effective labeling efficiency in MINFLUX 3D data may be slightly reduced due to the more stringent requirements for successful MINFLUX 3D localization.

Discussion

The isotropic 3D resolution approaching the single digit nanometer scale achievable with MINFLUX microscopy is a significant advance over previous optical super-resolution techniques that opens the door to truly molecular scale imaging in the heart. The higher resolution available with MINFLUX prompted us to re-evaluate the labeling, imaging and analysis processes involved in fluorescence imaging of RyR2s in HEK293 cells and adult mouse ventricular myocytes. Our new data supports a revised interpretation of the relationship between prior RyR2 data from EM tomography and super-resolution fluorescence microscopy that resolves some previously noted apparent discrepancies.

Imaging RyR2s with 3D MINFLUX microscopy

Use of small markers and detection of RyR2 subunit locations

MINFLUX is the first super-resolution microscopy modality that in our hands clearly shows a marked difference between a large marker system (primary secondary ABs) versus a more compact marker system such as the sdABs used here. The use of a small marker system was critical to enable the resolution of subunit locations. The resolution of subunit locations in turn enabled a novel strategy to quantify the labeling efficiency *in-situ*, similar to an approach previously employed for the imaging of nuclear pore complexes[21]. The new approach depends on the relatively large size of RyR2 tetramers in conjunction with the sufficiently small linkage error and high MINFLUX localization precision, which are expected to keep the total error (in 3D) below about 4 nm. Given the known location of GFP insertions which had been previously determined using cryo-EM[13,19] we show that estimating not only the precise location but also the 3D orientation of RyR2 tetramers in intact cells becomes feasible. Currently the effective labeling efficiency of subunits appears in practice too low to determine the 3D orientation for a sizable fraction of the RyR2s in a cell. Assuming that increasing labeling efficiency is essentially a biochemical "engineering problem", retrieving orientation information for RyR2 tetramers *in-situ* is an exciting prospect of MINFLUX and related molecular imaging techniques that may also be applicable to other large protein complexes, such as other multi-subunit ion channel complexes.

To reach the full potential of nanometer resolution fluorescence imaging the utility of a precisely known labeling location is demonstrated here. This is achievable using molecular tagging as with the fluorescent protein tags employed here or other small tags such as SNAP, Halo[22] and ALFA tags[23]. Insertion of these tags is readily achievable using molecular biology approaches and has the additional advantage that well characterised markers can be employed. A potential complication in practice may be the insertion into adult cardiac myocytes which generally requires viral delivery and for physiologically most relevant results will often involve generating a suitable genetically modified organism[8,24].

MINFLUX effective labeling efficiency

A novel aspect of the super-resolution imaging workflow shown here is an explicit estimate of effective labeling efficiency. Assumptions of "high labeling efficiency" often implicitly made in previous fluorescent imaging studies have recently been more systematically investigated in super-resolution microscopy[21] because labeling efficiency is becoming more important as spatial resolution approaches the molecular scale. While subunit labeling efficiencies between 10 and 15% may seem low, these values correspond to RyR2 labeling efficiencies of 34-48%, i.e., while the labeling is not complete, a substantial fraction of all RyR2s will be detected and sampled in MINFLUX 3D imaging with sdABs.

The effective labeling efficiency depends not only on successful "chemical" labeling by the marker but also on successful detection of the marker-attached fluorochromes during MINFLUX imaging. This latter condition depends on photo-switching and localization with the MINFLUX doughnut against backgrounds in the sample. These stringent requirements likely contribute to lowering the total probability of detecting a labeled RyR2 subunit. Consistent with this idea, the labeling efficiencies in myocytes are slightly lower than in HEK293 cells,

likely because of the optically more complex nature of these comparatively large diameter cells (~20 µm) which give rise to higher background signals, as well as the fact that the anti-tagRFP sdABs use X2 labeling rather than X4 labeling (which was the approach used with anti-GFP sdABs, see Supp. Fig. 3 and Methods).

Since previous RyR2 super-resolution studies typically used primary/secondary antibodies, we also tested if the labeling efficiency of the sdAB markers used here are disproportionally lower. For that purpose, we used "conventional" DNA-PAINT 2D imaging in a TIRF configuration to image RyR2s in peripheral couplings in mouse myocytes. We adopted this system, rather than MINFLUX microscopy, to remove the factor of "successful MINFLUX localization" and simplify comparison with previous studies. The distances between punctate labeling as a measure of labeled RyR2 density is similar between AB labeled and sdAB labeled samples (34 versus 38 nm) hinting at only moderate reduction in labeling efficiency when using sdABs. Comparison with MINFLUX imaging of sdAB using the same "blob-distance" metric suggests an again slightly lower efficiency given a blob distance of 42 nm, consistent with the idea that the more stringent requirements for successful localization are an additional factor in effective labeling efficiency.

Impact of Resolution of MINFLUX on RyR2 imaging

A remarkable property of MINFLUX is the essentially isotropic 3D resolution that it achieves when operated with a 3D doughnut[10] (see also our Fourier Shell Correlation Resolution measurements in Supp. Fig. 2 which confirm near isotropic resolution). This may be rivalled by existing 4PI SMLM approaches[14,25] but at the cost of the complexity of working with opposing objectives. The single objective design of 3D MINFLUX microscopy markedly simplifies the preparation and mounting of biological samples, a factor which in our experience is difficult to overestimate. The high, near isotropic 3D resolution enabled the quantification of the intrinsic three-dimensional nature of RyR2 clusters which was previously difficult to quantify using other optical super-resolution imaging techniques. In addition, the high 3D resolution with localization precisions on the order of 2 nm (once raw MINFLUX localizations are combined) is critical for the labeling efficiency algorithm that we developed and, given higher labeling efficiency aimed for in future, will be vital for routinely determining 3D orientation of RyR2 tetramers inside cells.

Insights from MINFLUX fluorescent RyR2 imaging

Quantitative analysis of the information available via MINFLUX 3D imaging revealed several complexities. The nanometre scale imaging of RyR2s by MINFLUX emphasizes that we do not collect data that directly shows protein locations but rather information on specific locations on those proteins, potentially offset by marker size (linkage error). Ideally, as is the case here, we know where on the large target protein, the RyR2 tetramer, these markers attach. Reconstructing the underlying protein distribution at the molecular scale requires further data processing and, in the case shown here, suggests that effects arising from labeling efficiency need to be considered.

Our analysis of clustering algorithm behaviour when subunit locations are missing (due to incomplete labeling) shows that clustering parameters may need to be adjusted to correctly group localizations (see Methods and Supp. Fig. 7). Only then can a correction for labeling efficiency be meaningfully applied to determine the "true" underlying cluster size as otherwise clusters would appear artificially fragmented. Based on these arguments, we adopted a DBSCAN radius of 100 nm to correctly reconstruct clusters that would be grouped together with a much tighter 40-50 nm DBSCAN radius if subunit labeling were complete.

We used previous data from EM tomography studies[4,20] and simulated how cluster layouts obtained from EM tomography would appear in MINFLUX 3D imaging with ~15% subunit labeling efficiency. The appearance of the simulated subunit location data is very similar to the actual MINFLUX data we obtained. This suggests a resolution to apparent discrepancies between RyR2 distribution patterns from super-resolution and EM data, where EM data from tomograms appeared to indicate a more dense packing of RyR2s[4,20] than observed in super-resolution imaging studies[2]. According to our new data this can be largely explained by labeling efficiency effects. Importantly, since MINFLUX 3D imaging provides a direct way to estimate labeling efficiency *in-situ* this now provides a way to use the complementary data provided by fluorescence and EM imaging to help reconstruct the true underlying RyR2 distribution characteristics from MINFLUX data. Note that available high resolution EM data has been generally restricted to internal couplings rather than the peripheral couplings imaged here. Our interpretation therefore hinges on the assumption that RyR2 packing in peripheral couplings is broadly similar. Our current investigation was limited to peripheral couplings since the long-term

stabilisation system (see Methods) required nanoparticles present as fiducials on the coverslip surface to be in focus, a constraint that we aim to relax in future experiments. This would enable the imaging of internal couplings with their more complex 3D structure using the isotropic resolution of 3D MINFLUX imaging. We suggest that with the rapid growth of volume EM imaging approaches[26] and true molecular scale fluorescence imaging (as exemplified by MINFLUX microscopy) there will be increasingly important synergies between fluorescent and EM approaches to RyR2 imaging. The MINFLUX based methods we introduce here provide advantages for applications in cardiac molecular imaging because of the much higher throughput that is achievable (both in terms of sample preparation, imaging and data analysis), the ability to extend this to proteins not easily discerned in EM data and, in principle, compatibility with live cell imaging.

Previous data on RyR2 clusters in peripheral couplings, albeit in rat ventricular myocytes, provided a mean of 8.8 RyR2s/cluster estimated with 2D DNA-PAINT[2] versus a mean of 7.9 RyR2s/cluster determined using 3D MINFLUX in mouse myocytes here. The values may not be directly comparable as 2D imaging was used previously (which would tend to overestimate cluster sizes) and the cluster algorithm was quite different (using thresholding of rendered 2D DNA-PAINT data) while labeling efficiency was not measured. More directly comparable are the MINFLUX imaging results of RyR2s stably expressed in HEK293 cells versus the clustering observed in mouse myocytes. RyR2 clusters in HEK293 cells had slightly smaller mean cluster size (~6.3 RyR2s).

What is a RyR2 cluster?

A key goal in grouping RyR2s into clusters is to identify groups of receptors that generally activate in unison to give rise to Ca^{2+} sparks and similar local release events. Due to calcium-induced calcium release these functional groups are generally formed by RyR2s in close proximity and thus approaches to group RyR2s into clusters according to a distance criterion have been widely used. There have been debates on the suitable distance "threshold" for grouping into clusters, with distances between 30 to 50 nm for clusters[3] and 100-150 nm for superclusters most often used[3,27,28]. Choices are typically guided by mathematical modeling and inspection of the more detailed models suggests that the distance between RyR2s alone may be insufficient to accurately predict the functional coupling between RyR2s. For example, the geometry of the local junctional space may affect the effective coupling between RyR2s, i.e. groups of RyR2s located within the same junction may gate very differently from groups separated by a region of cytosolic space[7,29,30]. The data from MINFLUX experiments presented here provides additional factors to consider when grouping RyR2s into clusters. As indicated above there is an interaction between the degree of labeling and the effective distance threshold used for clustering that has previously not been considered. To some extent effects of limited labeling efficiency may have been implicitly mitigated in previous super-resolution studies due to lower resolution "filling in gaps", an idea to explicitly evaluate in future comparison experiments. MINFLUX 3D imaging is capable of multi-channel imaging and therefore simultaneous imaging of local cellular compartment architecture may become accessible. In conjunction with such molecular resolution data and mathematical modelling as well as correlative functional studies[9,8,31], MINFLUX 3D imaging lays out a clear path to arrive at more precise and functionally relevant criteria to determine RyR2 functional groupings and refine our understanding of the RyR2 cluster concept for cardiac Ca^{2+} signalling.

Conclusion

MINFLUX 3D imaging provides a powerful new way to obtain molecular scale data on RyR2 distribution in cardiac cells with isotropic nanometre resolution. The new information available from 3D MINFLUX imaging of RyR2s will be useful for the construction of more detailed mathematical models and improve our understanding of Ca^{2+} signalling in the cardiac dyad. In addition, 3D MINFLUX imaging of RyR2 distribution within cells constitutes a more sensitive assay of nanoscale structure of cardiac myocytes than previously available super-resolution methods and should be used to refine observations of alterations in cardiac patho-physiology[5,7].

Given the multi-channel imaging capability of 3D MINFLUX imaging there is great scope for future studies that combine 3D distribution information from other Ca^{2+}-handling proteins and structures, such as transverse tubules and SR shape markers as well as other ion channels while aiming to maximise labeling efficiency.

Methods

Preparation of HEK-293 cells stably expressing $RyR2_{D4365\text{-}GFP}$ for MINFLUX imaging

HEK293 cells stably expressing inducible $RyR2_{D4365\text{-}GFP}$[13] were grown at 37°C with 5% CO_2 in Dulbecco's Modified Eagle's Medium – high glucose (Sigma), supplemented with 5% fetal bovine serum (Gibco) and 1% Antibiotic-Antimycotic (Gibco).

HEK293 $RyR2_{D4365\text{-}GFP}$ cells were seeded on precleaned coverslips treated with 0.1% Poly-l-lysine for 10min. After 1-2 days, the expression of $RyR2_{D4365\text{-}GFP}$ was induced by 1µg/ml doxycycline. 24h after the induction, cells were fixed with 4% PFA in PEM buffer [32] (80mM PIPES, 5mM EGTA, 2mM $MgCl_2$, pH 6.8) with 4% sucrose at RT for 10min. Coverslips with fixed cells were mounted in custom made slide chambers made from acrylic[33]. After three quick washes with PBS, fixed cells were blocked in 2.5% BSA with 0.1% Triton for 1h.

For direct labeling of GFP residues on $RyR2_{D4365\text{-}GFP}$, cells were incubated with a 1:500 dilution of FluoTag-X4 Anti-GFP (NanoTag Biotechnologies), coupled with an Alexa Fluor 647 dye for 1h at RT in solution containing 2% BSA, 2% NGS, 0.05% Triton X-100 and 0.05% sodium azide in PBS, followed by 3-4 washes with PBS.

For control experiments, the cells were prepared as described above, only the $RyR2_{D4365\text{-}GFP}$ expression was not induced by omission of doxycycline. Fixation and staining with FluoTag-X4 Anti-GFP was carried out as above.

For immunolabeling of the RyR, fixed HEK293 $RyR2_{D4365\text{-}GFP}$ cells were incubated with MA3-916 RyR2 monoclonal antibody (Invitrogen) diluted 1:100 at 4°C overnight in the same solution as above. The next day, samples were rinsed 3-4 times with PBS every 10 min and incubated with a 1:100 dilution of Alexa Fluor 647 secondary antibody (A-21235, Invitrogen) for 2h at RT, followed by a final round of PBS washing.

For immunolabeling of the ER protein reticulon 4B (Rtn4B), essentially the same protocol was applied as for RyR2 labeling. Rtn4B was stained with 10µg/ml of a Nogo-B antibody (AF6034, BioTechne) followed by Alexa Fluor 647 secondary antibody (A-21448, Invitrogen) diluted 1:100, with PBS washes as above.

Cardiac myocyte isolation from PA-RFP RyR2 mice

PA-RFP RyR2 mice that harbour PA-TagRFP inserted after T1365, within exon 31 of the mRyR2 gene on chromosome 13 as described[8], were housed at the University of Oslo and used to provide isolated myocytes. Single cardiomyocytes were isolated as previously described[34]. Briefly, the mice were first anesthetized by isoflurane inhalation before being euthanized by cervical dislocation. The heart was rapidly excised and cannulated on a constant flow Langendorff perfusion system. Up to 10 mL of an isolation buffer containing 130 mM NaCl, 5.4 mM KCl, 0.5 mM $MgCl_2$, 0.4 mM NaH_2PO_4, 25 mM HEPES and 5.5 mM D-glucose (pH adjusted to 7.4 using NaOH) was first used to flush the heart of blood. Once fluids ran clear the perfusion was switched to an isolation buffer which included 2 mg/mL collagenase type II (Worthington Biochemical, catalog: LS004176) for 7 minutes at 2 mL/min. After digestion the heart was cut down into isolation buffer containing 1 mg/mL bovine serum albumin (BSA) and the left ventricle diced into chunks. This solution was then filtered through a 200 µm filter mesh (SEFAR S-TEX PET 200), the cardiomyocytes were sedimented and the Ca^{2+} concentration gradually increased (0.1, 0.2, and 0.5 mM). Cells were then fixed with 4% PFA for 10 minutes at room temperature (RT). A 2 mM glycine solution was used to quench the cells for 1 hour at RT.

Labeling of myocytes from PA-RFP RyR2 mice for MINFLUX and widefield DNA-PAINT imaging

Cardiomyocytes were labeled in suspension. First, cells were permeabilized with 0.1% Triton X-100 for 10 minutes in 500 µL eppendorfs. The cardiomyocytes were centrifuged at 3k rpm for 3 minutes, the supernatant removed and blocked with 1% BSA in PBS for 1 hour. For MINFLUX imaging, cells were incubated 1:50 with FluoTag®-X2 anti-TagFP for 2 hours at RT. For comparison widefield DNA-PAINT imaging, myocytes were incubated 1:200 with Massive-Tag-Q anti-TagFP single domain antibody (Massive-Photonics) containing 'docking site 3' for 2 hours at room temperature in an incubation solution containing 2% BSA, 0.05% Triton X-100, 0.05% sodium azide in PBS. Samples were washed >3 times in PBS before being allowed to settle onto precoated 0.05% poly-l-lysine No 1.5 coverslips attached to custom-made open top chambers for easy access to solution changes[33]. For comparison DNA-PAINT experiments, involving primary and secondary antibodies, after the samples were blocked the cells were incubated with a ryanodine receptor monoclonal antibody (C3-33) (MA3-916, Invitrogen) overnight at 4˚C, 1:200 dilution in incubation solution. Samples were washed 3

times in PBS before being incubated with custom conjugated oligonucleotides (IDT) to AffiniPure goat anti-mouse IgG (H+L) secondary antibodies (Jackson ImmunoResearch) for 2H at RT, 1:200 in incubation solution. Finally, samples were washed in DNA-PAINT buffer made from PBS containing a total concentration of 750 mM NaCl. Cells were then added to poly-L-lysine coverslips as before.

Custom Oligonucleotide-antibody conjugation

Docking strands were purchased from Integrated DNA Technologies (Coralville, Iowa, United States) with 5' azide and 3' Cyanine 3 dye modifications. Imagers were purchased from Eurofins Genomics (Ebersberg, Germany) with 3' ATTO 655 modification. All oligos were HPLC purified and shipped lyophilized. Oligos were reconstituted in PBS at 100 µM and stored at -20˚C. The conjugation of oligo to antibody followed a click-chemistry protocol. Briefly, AffiniPure goat anti-Mouse IgG (H+L) secondary antibodies (115-005-003, Jackson ImmunoResearch) were incubated with DBCO-Sulfo-NHS ester (CLK-A124-10, Jena Bioscience) for 45 minutes. The reaction was stopped with 80 mM Tris-HCl for 10 minutes. The antibody-DBCO mixture was filtered using 7k MWCO Zeba Spin Desalting columns (Thermo Scientific) and the resulting antibody-DBCO was incubated with docking strand D2 (see Table 1) overnight at 4˚C. Finally, the conjugation mixture was purified using Amicon Ultra-0.5 (UFC5100, Merck) and measured using an Implen-N60 touch spectrophotometer (Fisher Scientific) to confirm >1 oligo conjugation per antibody.

Sample mounting for MINFLUX Microscopy

For active sample-stabilization during MINFLUX experiments, 150 nm colloid gold beads (BBI Solutions, EM.GC150) were used similarly, as fiducial markers[35]. Gold beads were added undiluted to the samples prior to imaging and allowed to settle for 5-10 minutes. Excess fiducials were removed with several washes in PBS. Samples were finally mounted in GLOX buffer (50 mM TRIS/HCl, 10 mM NaCl, 10% (w/v) Glucose and 64 µg/ml catalase, 0.4 mg/mL glucose oxidase, 10 - 25 mM MEA, pH 8.0)[35]. Samples were made airtight with a glass coverslip over the chamber and sealed with twinsil (picodent).

MINFLUX 3D imaging

Samples were imaged on an Abberior Instruments MINFLUX microscope that was equipped with a 642 nm excitation laser and a 405 nm activation laser. It could be run in confocal and MINFLUX imaging modes using a SLM-based beam shaping module and an EOD-based scanner for precision scanning (used in MINFLUX mode), similar as previously described[36,37]. Emitted fluorescence signals were measured using two photon-counting avalanche photodiodes and suitable fluorescence filters (650 -750 nm). In addition to MINFLUX modes, the microscope allows epifluorescence and 488 nm and 640 nm excitation confocal imaging acquisition. This was sometimes used to identify structures based on Alexa Fluor 488 labeling (control experiments in HEK293 cells lacking RyR2s) or Alexa Fluor 647 nm labeling (when using sdABs conjugated to Alexa Fluor 647). To enable measurements with molecular precision, the Abberior MINFLUX microscope is equipped with a reflection-based stabilization unit, based on a 980 nm laser. It features real-time feedback that dynamically adjusts a 3-axis nano-positioning stage to fix the sample position with respect to the objective lens with standard deviations typically below 1 nm over minutes and up to hours under normal laboratory conditions[36] (if mechanical agitation of the microscope by external sources are kept at a reasonably low level). To compensate changes in environmental conditions (especially temperature) that might manifest as a residual system drift, a beam line monitoring mode can be activated (in addition to the simultaneously operating real-time feedback stabilization) by selecting several in-focus gold nanoparticles whose position is tracked over time. The particle-averaged tracking information from these nanoparticles is then used to measure and correct focus drift by subtracting the apparent nanoparticle trajectory from the localization coordinates. Beam line monitoring can be maintained over hours and keeps drift induced position errors typically below 1.5 nm. The current implementation of beam line monitoring requires nanoparticles to be in focus so that the MINFLUX imaging volume in practice needs to be close to the coverslip interface during operation as most gold nanoparticles attach on the coverslip.

DNA-PAINT imaging

Data was acquired using a modified Nikon Eclipse Ti-E inverted microscope (Nikon, Tokyo) with a fixed 60x 1.49 NA APO oil immersion TIRF objective (Nikon, Tokyo), as previously described[38]. Images were captured with an Andor Zyla 4.2 sCMOS camera (Andor, Belfast) utilizing a 100 ms integration time. Focus was

controlled using a piezo objective scanner (P-725, Physik Instrument, Karlsruhe). For widefield fluorescence, a tunable LED-light source (CoolLED, Andover) was used to aid cell selection and confirm proximity of 200 nm red fluorescent beads (fiducials) within the imaging region. These fluorescent markers were later used to correct for any lateral drift experienced over the course of data acquisition. Active z-stabilization was maintained whilst imaging through the use of an auxiliary camera monitoring transmitted light at a non-interfering wavelength from the super-resolution channel[2,38]. A continuous wave 647 nm diode laser (Omikron LuxX, Rodgau) was used to excite ATTO 655 imagers for single molecule measurements. Single molecule data was recorded using the open-source python software package called PyME[39] (Python Microscopy Environment, https://github.com/python-microscopy/python-microscopy). Samples for DNA-PAINT were imaged in PBS containing a total concentration of 750 mM NaCl. The imagers, either 'imager 3' (Massive Photonics) or A2 (see Table 1), were diluted to 0.6 nM in this solution depending on whether the sdAb or the primary/secondary antibody system was used.

Analysis of image data

Analysis of 3D MINFLUX data

Raw MINFLUX localizations were exported from Abberior Instruments Imspector software[36] and converted using PYME routines into a suitable format for importing into PYMEVisualize[39] for further processing. *Raw MINFLUX localizations* were processed by combining localizations to represent different aspects of the underlying structures, including *dye locations*, *dye groups* and *subunit locations*. *Dye locations* were obtained from *raw MINFLUX localizations* to obtain locations that each represent a dye molecule location during a single "blink" event. *Dye groups* of closely spatially aggregated *dye locations* (on a scale similar to the size of an RyR2) were determined by DBSCAN clustering and qualitatively analysed using data from primary/secondary antibody labeling versus data from sdAB labeling of GFP. To obtain unique *subunit locations* we used an approach similar to the procedure used previously to reassign filtered MINFLUX localizations to individual molecules[12]. These *subunit locations* were obtained by combining *dye locations* that (1) arose from dye molecules that reappear due to blinking or (2) correspond to dye molecules on the same sdAB or, finally, (3) arose from two sdABs on the same GFP subunit. *Subunit locations* in turn were processed with an algorithm that we developed, to estimate the labeling efficiency of subunits by sdABs. In addition, *subunit locations* were subjected to cluster analysis by DBSCAN clustering with the aim to characterise the underlying RyR2 clustering properties. Further details on the procedures to obtain the locations, groupings and clusters mentioned above are described in the supplementary methods.

Analysis of widefield DNA-PAINT data

Single molecule localization DNA-PAINT data were rendered using PYMEVisualize[39] into TIFF images with a pixel size of 5 nm by jittered triangulation[40]. A PyME object finding module (PYME.localization.ofind3d) was used to detect puncta within these images using a threshold of 1.0 and blur size 2.0. The 2D coordinates of the detected puncta were used to determine their nearest neighbor (NN) distances.

Statistical comparisons

A two-sample t-test was conducted on the subunit labelling efficiencies estimated from HEK293 RyR2 and myocyte RyR2 MINFLUX data using the R programming language in a Jupyter notebook environment. To assess the suitability of the two-sample t-test the normality assumption and the homogeneity of variances between the two datasets were first evaluated using the Shapiro-Wilk normality test and a Levene's test for both mean and median.

For comparing nearest neighbor puncta distances, we conducted statistical comparisons implemented in the Python programming language within a Jupyter notebook environment. First, a one-way ANOVA test was performed using the `scipy.stats` module to assess the null hypothesis that the means of the three groups tested were equal. The result suggested that at least one of the groups exhibited a significantly different mean compared to the others. Pairwise differences were further investigated using the `statsmodels.api` library utilizing the `pairwise_tukeyhsd` function. This function implements the Tukey's Honestly Significant Difference (Tukey HSD) test and compares all possible pairs of group means to identify statistically significant differences. The p-values were then recorded.

Acknowledgements

We acknowledge project support from the Swiss National Science Foundation (SNSF 310030_208109 to C. S.). The equipment was supported by the SNSF (SNSF R'Equip 316030_213543 to C. S.), the University of Bern Innovation Fund and the Faculty of Medicine. P. P. J. acknowledges partial project support by the Health Research Council of New Zealand (HRC #20/370). W. E. L. was supported by the Norwegian Research Council (grant number 287395). We thank Jia Li for assistance with cell isolations.

Table. 1. List of oligonucleotide sequences used for conventional 2D DNA-PAINT imaging.

Name	**Sequence 5' -> 3'**
Docking strand, D2	[AzideN] TTT TAG GTA AAT TTT GAT TGT GAG GAA G [Cy3]
Imager strand, A2	TAC AAT CAA A [ATTO 655]

Author contributions

Conceptualization: C.S, W.E.L, P.P.J. **Data curation:** C.S, I.J, A.H.C. **Formal analysis:** C.S, A.H.C. **Funding acquisition:** C.S. **Investigation:** I.J, A.H.C, A.M, E.L. **Methodology:** C.S, I.J, A.H.C, A.M, E.L. **Project administration:** C.S. **Resources:** I.J, P.P.J, W.E.L, C.S. **Software:** C.S, A.H.C. **Supervision:** C.S. **Validation:** A.M, A.H.C. **Visualization:** C.S, A.H.C, A.M. **Writing:** All authors contributed to the writing of the manuscript.

Competing interests

The authors declare that they have no competing interests in the production and presentation of results. I.J. works at Abberior Instruments that develops and manufactures superresolution fluorescence microscopes, including the 3D-MINFLUX system used here.

References

1. Shen, X. *et al.* 3D dSTORM imaging reveals novel detail of ryanodine receptor localization in rat cardiac myocytes. *J. Physiol.* **597**, 399–418 (2019).
2. Jayasinghe, I. *et al.* True Molecular Scale Visualization of Variable Clustering Properties of Ryanodine Receptors. *Cell Rep.* **22**, 557–567 (2018).
3. Baddeley, D. *et al.* Optical single-channel resolution imaging of the ryanodine receptor distribution in rat cardiac myocytes. *Proc. Natl. Acad. Sci. U. S. A.* **106**, 22275–22280 (2009).
4. Asghari, P. *et al.* Nonuniform and variable arrangements of ryanodine receptors within mammalian ventricular couplons. *Circ. Res.* **115**, 252–262 (2014).
5. Shen, X. *et al.* Prolonged β-adrenergic stimulation disperses ryanodine receptor clusters in cardiomyocytes and has implications for heart failure. *eLife* **11**, e77725 (2022).
6. Cabra, V., Murayama, T. & Samsó, M. Ultrastructural Analysis of Self-Associated RyR2s. *Biophys. J.* **110**, 2651–2662 (2016).
7. Kolstad, T. R. *et al.* Ryanodine receptor dispersion disrupts Ca2+ release in failing cardiac myocytes. *eLife* **7**, e39427 (2018).

8. Hou, Y. *et al.* Live-cell photoactivated localization microscopy correlates nanoscale ryanodine receptor configuration to calcium sparks in cardiomyocytes. *Nat. Cardiovasc. Res.* **2**, 251–267 (2023).
9. Hurley, M. E. *et al.* A correlative super-resolution protocol to visualise structural underpinnings of fast second-messenger signalling in primary cell types. *Methods* **193**, 27–37 (2021).
10. Gwosch, K. C. *et al.* MINFLUX nanoscopy delivers 3D multicolor nanometer resolution in cells. *Nat. Methods* **17**, 217–224 (2020).
11. Weber, M. *et al.* MINSTED fluorescence localization and nanoscopy. *Nat. Photonics* **15**, 361–366 (2021).
12. Pape, J. K. *et al.* Multicolor 3D MINFLUX nanoscopy of mitochondrial MICOS proteins. *Proc. Natl. Acad. Sci.* **117**, 20607–20614 (2020).
13. Liu, Z., Zhang, J., Li, P., Chen, S. R. W. & Wagenknecht, T. Three-dimensional Reconstruction of the Recombinant Type 2 Ryanodine Receptor and Localization of Its Divergent Region 1*. *J. Biol. Chem.* **277**, 46712–46719 (2002).
14. Wang, J. *et al.* Implementation of a 4Pi-SMS super-resolution microscope. *Nat. Protoc.* **16**, 677–727 (2021).
15. Liu, S., Hoess, P. & Ries, J. Super-Resolution Microscopy for Structural Cell Biology. *Annu. Rev. Biophys.* **51**, annurev-biophys-102521-112912 (2022).
16. Ostersehlt, L. M. *et al.* DNA-PAINT MINFLUX nanoscopy. *Nat. Methods* **19**, 1072–1075 (2022).
17. Muyldermans, S. *et al.* Camelid immunoglobulins and nanobody technology. *Vet. Immunol. Immunopathol.* **128**, 178–183 (2009).
18. Hou, Y. *et al.* Correlating Calcium Sparks and Ryanodine Receptor Localization in Live Cardiomyocytes. *Biophys. J.* **118**, 567a (2020).
19. Liu, Z., Zhang, J., Wang, R., Wayne Chen, S. R. & Wagenknecht, T. Location of Divergent Region 2 on the Three-dimensional Structure of Cardiac Muscle Ryanodine Receptor/Calcium Release Channel. *J. Mol. Biol.* **338**, 533–545 (2004).
20. Asghari, P. *et al.* Cardiac ryanodine receptor distribution is dynamic and changed by auxiliary proteins and post-translational modification. *eLife* **9**, e51602 (2020).
21. Thevathasan, J. V. *et al.* Nuclear pores as versatile reference standards for quantitative super-resolution microscopy. *Nat. Methods* **16**, 1045–1053 (2019).
22. Fornasiero, E. F. & Opazo, F. Super-resolution imaging for cell biologists: Concepts, applications, current challenges and developments. *BioEssays* **37**, 436–451 (2015).

23. Götzke, H. *et al.* The ALFA-tag is a highly versatile tool for nanobody-based bioscience applications. *Nat. Commun.* **10**, 4403 (2019).
24. Hiess, F. *et al.* Distribution and Function of Cardiac Ryanodine Receptor Clusters in Live Ventricular Myocytes. *J. Biol. Chem.* **290**, 20477–20487 (2015).
25. Shtengel, G. *et al.* Interferometric fluorescent super-resolution microscopy resolves 3D cellular ultrastructure. *Proc. Natl. Acad. Sci. U. S. A.* **106**, 3125–3130 (2009).
26. Collinson, L. M. *et al.* Volume EM: a quiet revolution takes shape. *Nat. Methods* **20**, 777–782 (2023).
27. Sobie, E. A. *et al.* The Ca2+ leak paradox and "rogue ryanodine receptors": SR Ca2+ efflux theory and practice. *Prog. Biophys. Mol. Biol.* **90**, 172–185 (2006).
28. Macquaide, N. *et al.* Ryanodine receptor cluster fragmentation and redistribution in persistent atrial fibrillation enhance calcium release. *Cardiovasc. Res.* **108**, 387–398 (2015).
29. Mesa, M. H., Brink, J. van den, Louch, W. E., McCabe, K. J. & Rangamani, P. Nanoscale organization of ryanodine receptor distribution and phosphorylation pattern determines the dynamics of calcium sparks. *PLOS Comput. Biol.* **18**, e1010126 (2022).
30. Hoang-Trong, T. M., Ullah, A., Lederer, W. J. & Jafri, M. S. A Stochastic Spatiotemporal Model of Rat Ventricular Myocyte Calcium Dynamics Demonstrated Necessary Features for Calcium Wave Propagation. *Membranes* **11**, 989 (2021).
31. Hurley, M. E., White, E., Sheard, T. M. D., Steele, D. & Jayasinghe, I. Correlative super-resolution analysis of cardiac calcium sparks and their molecular origins in health and disease. *Open Biol.* **13**, 230045 (2023).
32. Jimenez, A., Friedl, K. & Leterrier, C. About samples, giving examples: Optimized Single Molecule Localization Microscopy. *Methods* **174**, 100–114 (2020).
33. Crossman, D. J., Hou, Y., Jayasinghe, I., Baddeley, D. & Soeller, C. Combining confocal and single molecule localisation microscopy: A correlative approach to multi-scale tissue imaging. *Methods* **88**, 98–108 (2015).
34. Hou, Y., Le, C., Soeller, C. & Louch, W. E. Protocol for the Isolation and Super-resolution dSTORM Imaging of RyR2 in Cardiac Myocytes. *BIO-Protoc.* **8**, e2952 (2018).
35. Balzarotti, F. *et al.* Nanometer resolution imaging and tracking of fluorescent molecules with minimal photon fluxes. *Science* **355**, 606–612 (2017).
36. Schmidt, R. *et al.* MINFLUX nanometer-scale 3D imaging and microsecond-range tracking on a common fluorescence microscope. *Nat. Commun.* **12**, 1478 (2021).

37. Grabner, C. P. *et al.* Resolving the molecular architecture of the photoreceptor active zone with 3D-MINFLUX. *Sci. Adv.* **8**, eabl7560 (2022).
38. Clowsley, A. H. *et al.* Repeat DNA-PAINT suppresses background and non-specific signals in optical nanoscopy. *Nat. Commun.* **12**, 501 (2021).
39. Marin, Z. *et al.* PYMEVisualize: an open-source tool for exploring 3D super-resolution data. *Nat. Methods* **18**, 582–584 (2021).
40. Baddeley, D., Cannell, M. B. & Soeller, C. Visualization of localization microscopy data. *Microsc. Microanal.* **16**, 64–72 (2010).